Extreme Mechanics Letters 59 (2023) 101957

Contents lists available at ScienceDirect

Extreme Mechanics Letters

journal homepage: www.elsevier.com/locate/eml

Magnetic field-induced asymmetric mechanical metamaterials

Quan Zhang [a,*], Andrei V. Cherkasov [a], Nitesh Arora [b], Gengkai Hu [c], Stephan Rudykh [a,b]

[a] School of Mathematical and Statistical Sciences, University of Galway, University Road, Galway, Ireland
[b] Department of Mechanical Engineering, University of Wisconsin – Madison, Madison, WI 53706, United States
[c] School of Aerospace Engineering, Beijing Institute of Technology, Beijing, 100081, China

ARTICLE INFO

Article history:
Received 14 October 2022
Received in revised form 15 December 2022
Accepted 3 January 2023
Available online 10 January 2023

Keywords:
Hard-magnetic soft materials
Magnetoactive mechanical metamaterials
Reconfigurable microstructures
Band gaps

ABSTRACT

We propose a magnetic field-induced asymmetric mechanical metamaterial. The tunable metamaterial integrates hard-Magnetic Active Elastomers (hMAEs) into the microstructural design combining snap-through, bi-stability, and local resonant effects. The proposed metamaterial design comprises resonating units made out of hMAE, and these units are supported by highly deformable curved beams connected with an elastomeric matrix. Activated by a magnetic field, the resonating units attain an unstable regime with dramatic configuration and stiffness variation. These controlled transformations significantly affect the elastic wave propagation. We illustrate that the proposed magnetoactive metamaterial enables bandgap tunability over a broadband low-frequency range. Thus, the proposed design allows remote and reversible control of the metamaterial performance. Moreover, the hMAE-based systems can incorporate the polarity and chirality stemming from the interaction of external magnetic fields and hMAE phases, giving rise to the unusual behavior of the metamaterial, and potentially enabling elastic cloaking.

1. Introduction

Elastic metamaterials [1] draw their performance from neat microstructures, giving rise to topological phase transitions, extreme (and negative) effective parameters, and the bandgap (BG) phenomenon. The potential metamaterial applications range from vibration isolation [2–5] and switching [6] to subwavelength waveguiding [7–9] and focusing [10], to the topological state of matter [11–15] that enables elastic wave flows immune to backscattering losses. Moreover, *soft* active materials offer ways to control the metamaterial performance through mechanical deformation [16,17] or external field activation [18–20], leading to reversible property changes and shape transformations. The transformative ability of magnetic active elastomers (MAEs) and their remote principle of actuation make them a promising material platform for *untethered* devices.

Typically, MAEs consist of magnetizable particles embedded in a soft matrix. The application of an external magnetic field produces complex interactions between the magnetized particles, resulting in overall material deformation and modification of the effective properties [21–24]. Furthermore, MAEs can be designed to capitalize on buckling or instability phenomena, triggering dramatic changes in material microstructures and, thus, producing reversible switches in material properties [25–28]. These so-called *soft*-Magnetic Active Elastomers contain active particles made of iron, soft ferrite, or iron–silicon alloys. These soft-magnetic materials are characterized by a low coercivity and do not retain remanent magnetization once the external magnetic field has been removed [29].

Recently, particles of high-coercivity ferromagnetic materials (such as NdFeB, hard ferrite, and alnico alloys) have been utilized to fabricate *hard*-Magnetic Active Elastomers (hMAEs) [30,31]. Once exposed to a large enough magnetic field and saturated, hard-magnetic materials retain their magnetization even after removing the external field. The high coercivity allows the hard-magnetic materials to sustain their remanent magnetization over a wide range of applied magnetic fields (that are below the coercive field strength). When the applied magnetic field is not aligned with the magnetization direction of the hard-magnetic particles, the induced magnetic body torque acts to align the particle's magnetization direction with the field direction. This microscopic effect leads to a macroscale response of the hMAE composite in the form of complex shape transformations at *low* magnetic fields [30–38]. Such rapid, reversible, and remotely-controlled shape-transforming behavior of hMAEs has enabled functionalities in areas such as soft robotics [39] and biomedical devices [40]. More recently, the hMAEs have been used for phononic crystal designs with tunable Bragg scattering BG whose operating frequency is defined by the unit cell length scale [34,41,42].

* Corresponding author.
E-mail address: quan.zhang@universityofgalway.ie (Q. Zhang).

https://doi.org/10.1016/j.eml.2023.101957

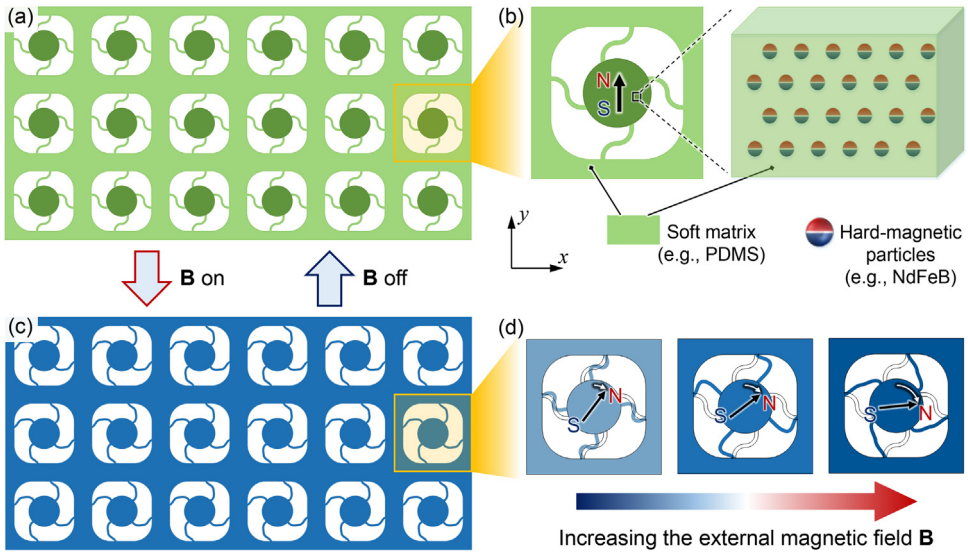

Fig. 1. Schematics of the magnetoactive elastic metamaterials. (a) The undeformed configuration comprises resonators embedded into a soft matrix. (b) The resonator unit cell consists of the hMAE core (with remanent magnetization in the $+y$ direction) connected to the matrix by the curved beams. (c) and (d) The magnetic-field activated configuration.

Here, we put forward a novel design of hMAE-based metamaterials functioning beyond the subwavelength limit. The microstructure and operating frequency of the proposed local resonant metamaterials can be tuned, through reconfigurable interactions between the magnetic domains remotely controlled by an external magnetic field. The tunability of the metamaterials is facilitated by the pre-designed snap-through and bistable system behavior. The proposed magnetoactive elastic metamaterials can achieve vibration mitigation over a broadband low-frequency range.

2. Results and discussions

Fig. 1 illustrates the proposed magnetoactive metamaterial design. The system consists of an array of resonators embedded into a matrix (Fig. 1a). The resonating cores are made of hMAE supported by four curved deformable beams. The resonating core can be fabricated by casting and curing the mixture of hard-magnetic particles (e.g., NdFeB) and the elastomer resin in molds. After being exposed to a large enough magnetic field and saturated, these cores maintain a remanent magnetization $\mathbf{M}$ (in the $+y$ direction, Fig. 1b). The application of an external magnetic field (whose direction is not aligned with $\mathbf{M}$, such as in the horizontal direction), induces the magnetic body torque $\boldsymbol{\tau} = \mathbf{M} \times \mathbf{B}$ acting to align the core's magnetization direction with the applied magnetic field (Fig. 1c and d). The induced rotation of the core leads to compression or stretching (depending on the direction of the external magnetic field) of the curved beams. Such field-induced deformation alters the stiffness of the beams and consequently the natural frequency of the resonators. Interestingly, the rotation of the core and the induced compression of the curved beam may result in snap-through and bistable behavior; in such an event, the curved beam will remain in the new stable configuration even after the external magnetic field is removed.

We start by investigating the effect of external magnetic fields on the deformation of the system. Consider the unit cell shown in Fig. 2a. The lattice constant is $L = 30.0$ mm and the radius of the hMAE core is $r = 6.0$ mm; the side length of the hollow rectangle is $l = 23.0$ mm, and the radius of its four arc chamfers is $R = 6.9$ mm. The thickness of the curved beam is $t = 0.8$ mm, and the horizontal distance between the two ends of the beam centerline is $W = 5.0$ mm (as illustrated by the upper panel in Fig. 2a). The centerline shape of the curved beam is obtained by chamfering the two right angles of the "N"-shaped polyline, and the radius of the two chamfers equals $W/2$. The distance between the common endpoint (point P) of the two arc chamfers and the center of the unit cell is $h = (l/2 + r)/2$.

The initial shear modulus and density of the matrix and beams are $G_0 = 200$ kPa and $\rho_0 = 1160$ kg/m^3 (corresponding to the commercial polydimethylsiloxane (PDMS) used in Ref. [40]), respectively. The hMAE core is modeled as PDMS doped with neodymium-iron-boron (NdFeB, with remanent magnetization $M_N = 640$ kA/m and density $\rho_N = 7610$ kg/m^3, see Ref. [40]) particles. The volume fraction of NdFeB particles in the hMAE core is denoted by ϕ; the remanent magnetization of the core is approximated as the volume average of the total magnetic moment of individual particles, i.e., $M = M_N\phi$. Following the Mooney model [43], the shear modulus of the hMAE core is estimated as $G(\phi) = G_0 \exp[2.5\phi/(1 - 1.35\phi)]$. Here, the NdFeB particle volume fraction of the hMAE core is taken to be $\phi = 0.2$; thus, the core is modeled with shear modulus $G = 396.7$ kPa, density $\rho = 2450$ kg/m^3, and remanent magnetization $M = 128$ kA/m.

To determine the magneto-mechanical response of the periodic system, a representative unit cell is constructed in 2D under the plane strain conditions, and periodic boundary conditions are applied to the boundaries of the unit cell [26]. The equilibrium equation and the magnetostatic equations are solved in COMSOL Multiphysics 6.0. The magneto-mechanical coupling is established via introducing the *total* stress depending on the magnetic field [41], namely

$$\boldsymbol{\sigma}_{total} = \boldsymbol{\sigma}_{el} + \frac{1}{\mu}\mathbf{B} \otimes \mathbf{B} - \frac{1}{\mu_r}\mathbf{M} \otimes \mathbf{B}, \tag{1}$$

where $\boldsymbol{\sigma}_{el}$ denotes the purely elastic stress component, μ is the material permeability, and $\mu_r = \mu/\mu_0$ (μ_0 is the permeability of the vacuum) is the relative magnetic permeability. The magnetic field $\mathbf{B}$ in the horizontal direction ($\mathbf{B} = B\mathbf{e}_1$, where $\mathbf{e}_1$ is the unit vector of the x-axis; see Fig. 1) is applied by specifying the magnetic scalar potential difference on the boundary of the unit cell. The mechanical response of the constitutive materials is described by the neo-Hookean model. The remanent magnetization in the core is assumed to be in the positive $+y$ direction (see Fig. 2a).

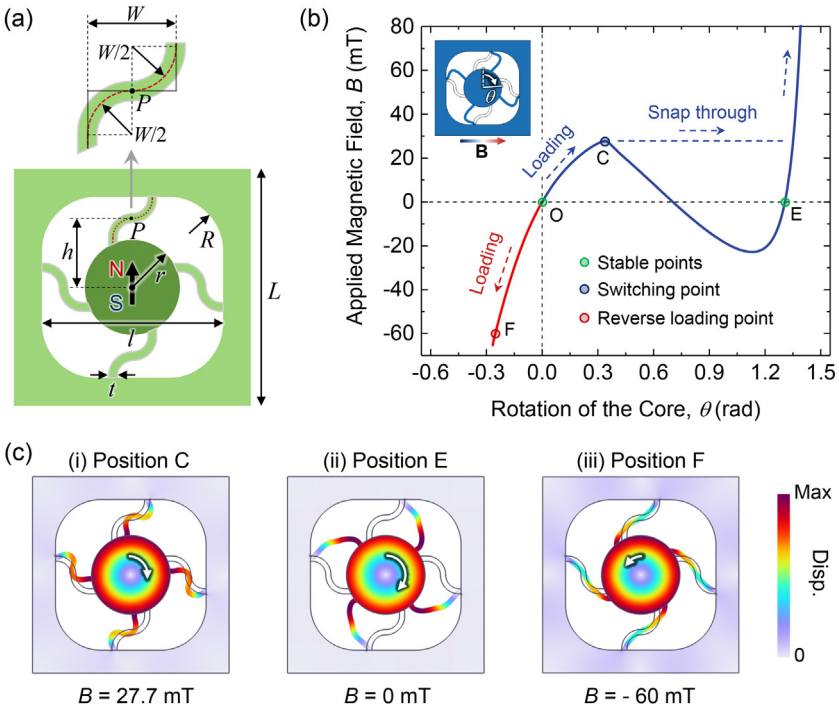

Fig. 2. Magnetic activation mechanism of the metamaterial. (a) Geometric parameters of the unit cell. (b) Magnetic field-induced rotation of the hMAE core. The blue curve corresponds to the compression of the curved beam (the core rotates clockwise). Snap-through occurs at the peak that is denoted as the switching point C (when the unit is activated by a magnetic field in the +*x* direction). The red curve corresponds to the stretch of the curved beam, corresponding to the counterclockwise rotation of the core under a magnetic field applied in the negative *x* direction. (c) The activated configurations correspond to states C, E, and F (marked in (b)). (For interpretation of the references to color in this figure legend, the reader is referred to the web version of this article.)

Fig. 2b displays the magnetic actuation of the metamaterials. The response curve is obtained by calculating the resultant magnetic field level B for varying core rotation angle θ. The angle θ is defined to be positive when the core rotates clockwise and negative otherwise. An extremum of magnetic field level B is observed at the peak denoted as position C, and the corresponding deformed configuration is shown in Fig. 2c(i). One can see that the curved beams are significantly compressed. If the metamaterial is activated by gradually increasing magnetic field in the +*x* direction, snap-through occurs at the switching point (position C) where the curve enters a negative stiffness regime. Moreover, there is a range of negative magnetic field (part of the blue curve — from 0.70 and 1.31 rad), indicating the bistable system behavior. As the magnetic field is gradually reduced to zero, the system becomes stable at position E (note the positive curve slope); the corresponding deformed configuration is presented in Fig. 2c(ii). The bistable characteristic provides a shape-locking mechanism for the design of magnetoelastic metamaterials. This mechanism allows the transformed microstructure to be preserved without a continuous application of the external magnetic field. Note that the transformed microstructure (position E) can reversibly recover to the initial configuration (position O) under the application of a magnetic field in the -*x* (negative) direction ($B < 0$). If the initial undeformed metamaterial is actuated by a magnetic field in the -*x* direction, the hMAE core rotates counterclockwise, and the beams are stretched (a typical deformed configuration is shown in Fig. 2c(iii)); in this case, no snap-through is observed.

Next, we consider how the snap-through and bistable behavior can be tuned through the geometry of the connected beams. Fig. 3a shows the variations in core rotation versus the applied magnetic field for the metamaterial with various beam thicknesses t. The results are shown for the metamaterial with the fixed beam centerline span $W/L = 0.15$ and the other geometric parameters remaining fixed, as considered in Fig. 2a. As the beam thickness t increases, the critical rotation angle (at which the snap-through happens) barely changes ($\theta \approx 0.32$ rad). Meanwhile, the magnetic field level (i.e., the local maxima in B) required to trigger the snap-through increases from 8.9 mT to 25.3 mT, as the thickness is increased from $t/L = 1/50$ to $t/L = 1/37.5$. We note that the beam thickness t almost does not affect the stability behavior of the system. In particular, the position of the (non-trivial) stable state barely changes. This is because the system stability behavior is mainly defined by the beam curvature (parameterized as the beam centerline span W). Fig. 3b illustrates the dependence of the magnetic field-induced core rotation behavior on the initial beam curvature W. The results are shown for the system with the fixed beam thickness $t/L = 1/37.5$. The critical rotation angle and the magnetic field level of the critical point (at the peak) change significantly with an increase in W. For instance, in the metamaterial system with $W/L = 1/30$, snap-through is triggered at the position with a rotation angle of 0.11 rad, and the required magnetic field level is 3.4 mT. By contrast, the rotation angle for triggering snap-through is increased to 0.22 rad in the system with $W/L = 1/12$, and the corresponding magnetic field level shifts to 13.5 mT. Moreover, the instability behavior undergoes a transition with an increase in W. For lower values of W (e.g., $W/L = 1/30$), the system exhibits snap-through but does not have the bistable range. Above a critical value of W (about $W/L \approx 1/16.5$), the magnetoactive system becomes bistable (e.g., $W/L = 1/12$).

Next, we investigate the effect of magnetic field-induced microstructure transformation on the propagation of small amplitude elastic waves. To this end, we calculate the dispersion relations for the periodic system using the eigenfrequency analysis in COMSOL Multiphysics 6.0, accounting for the effect of pre-deformation induced by magnetic fields. In the simulations, the material and geometric parameters are identical to those considered in Fig. 2.

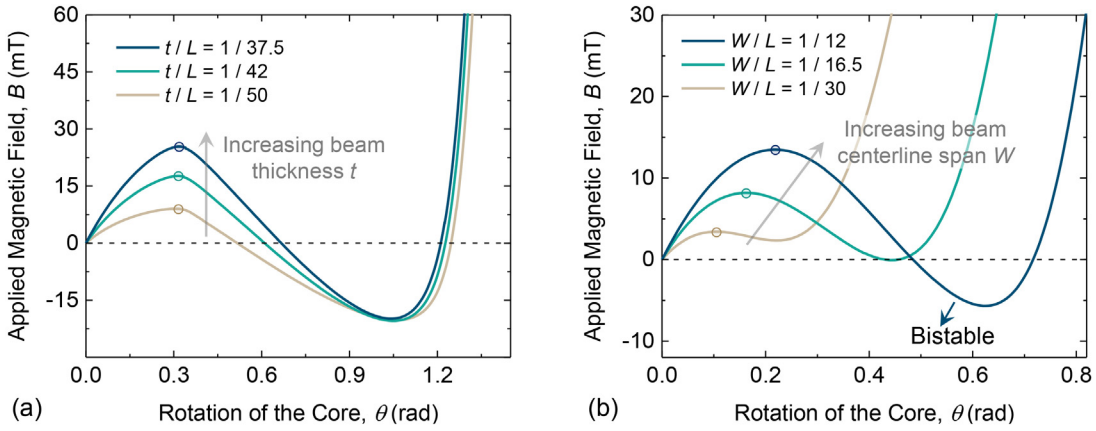

Fig. 3. Magnetic field-induced core rotation. (a) The effect of beam thickness t on the snap-through and bi-stability. (b) The effect of beam curvature W on the snap-through and bi-stability.

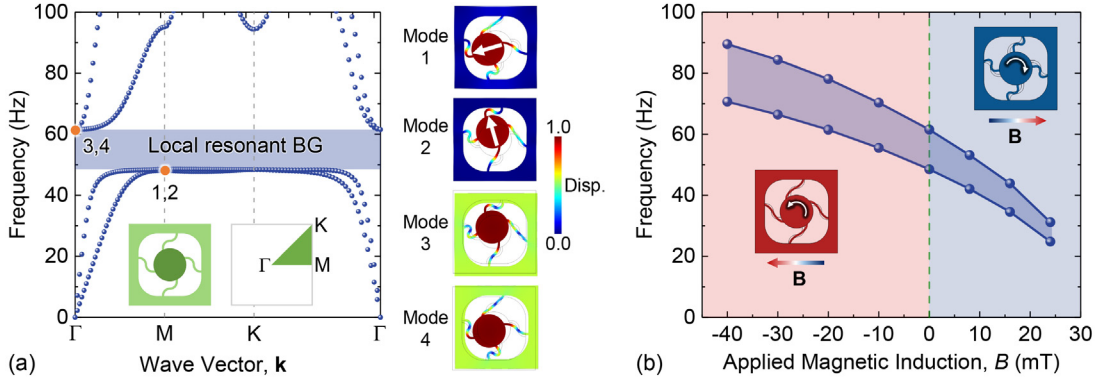

Fig. 4. Effect of the applied magnetic field on the local resonant BG. (a) The band structure of the magnetoactive elastic metamaterial in the inactivated configuration, with the first local resonant BG highlighted by the shaded area. (b) The evolution of the first local resonant BG with respect to the applied magnetic field.

The band structure of the periodic system in the undeformed state, together with four typical eigenmodes, is presented in Fig. 4a. The resonating core, together with the deformable curved beams, constitutes a classical local resonator. We can see that the first and second modes at M show a strong vibration localization, with the displacement concentrated in the resonator. By contrast, in the third and fourth modes, the displacement of the matrix is comparable to that of the resonator. Moreover, due to the chiral characteristics of the unit cell, the eigenmodes exhibit *elliptical* polarization instead of *linear* polarization. For instance, the first (second) local resonant mode at M (the corresponding wave vector is along the x-axis) is polarized in a direction close to the x- (y-) axis, rather than exactly along the x- (y-) axis, as shown by the white arrow in the eigenmode. The coupling between the local resonator and the propagating wave in the media generates a local resonant BG, as highlighted by the shaded area in Fig. 4a. The effect of the external magnetic field on the propagation of elastic waves is illustrated in Fig. 4b. Fig. 4b displays the variation of the local resonant BG frequency range with the level and direction of the applied magnetic field. Under the action of the magnetic field applied in the $+x$ direction, the curved beams experience compression, and their stiffness gradually reduces before reaching the critical switching point where the snap-through is triggered. Correspondingly, the local resonant BG is shifted to lower frequencies, as shown in the right half quadrant of Fig. 4b. By contrast, with the application of the magnetic field in the opposite direction ($-x$ direction), the beams are stretched, and their stiffness increases; therefore, the BG frequency range increases. Our results demonstrate that the proposed magnetoactive metamaterial can change its operating frequency on demand by remotely applied magnetic fields.

Finally, we calculate the transmittance spectra for the finite-size metamaterial sample (see Fig. 5a). The results are calculated for the numerical model comprising 10×1 unit cells, with periodic boundary conditions assigned on the upper and lower boundaries. First, a magnetic excitation in the horizontal direction is applied, and the metamaterial sample is pre-deformed; next, a harmonic perturbation at the left boundary of the deformed sample is imposed. The induced harmonic response at the right boundary is captured, and the transmittance spectrum is computed as the ratio between the output and input displacements, reported as $20 \log_{10} \|A_{out}(\omega) / A_{in}(\omega)\|$. The material and microstructure geometric parameters are identical to those considered in Fig. 2.

Fig. 5b displays the transmittance spectra of the metamaterial sample calculated at $B = 24$ mT, 0 mT, and -40 mT. In the inactivated state (i.e., $B = 0$ mT), a significant transmittance drop is observed between 49.1 Hz and 62.1 Hz (as highlighted by the green area). The starting frequency (that is 49.1 Hz) of the low transmittance area quantitatively agrees with the lower edge (that is 48.5 Hz) of the BG shown in Fig. 4a. In agreement with the independent BG calculation, the low transmittance range shifts when a magnetic field is applied. In particular, for $B = 24$ mT the drop in the transmittance is shifted to the range between 26.7 Hz and 32.6 Hz (the blue area in Fig. 5b), and for $B = -40$ mT, the transmittance drop is shifted to the range between 72.3 Hz and 90.7 Hz (the red area in Fig. 5b). Therefore, by continuously changing the applied magnetic field from -40 mT to 24 mT,

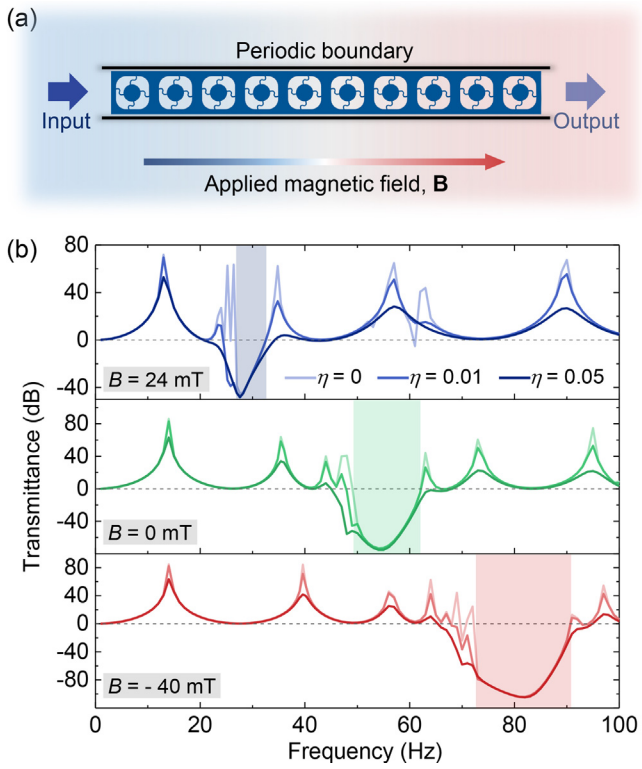

Fig. 5. Effect of the applied magnetic field on the transmittance spectra of finite-size magnetoactive metamaterial samples. (a) Schematics of the finite-size numerical model. (b) The transmittance spectra of a sample with ten unit cells under magnetic fields with different strengths and directions. Here η denotes the damping coefficient used in the numerical simulations. (For interpretation of the references to color in this figure legend, the reader is referred to the web version of this article.)

the attenuation performance can be achieved over a broadband low-frequency range from 26.7 Hz to 90.7 Hz.

The BG tuning effects may be affected by the damping of the soft matrix PDMS. To illustrate the effect, we calculate the transmittance spectra considering material damping, as shown in Fig. 5b. Here η denotes the damping coefficient. One can see that damping smoothens the resonant peaks with high transmittance. Moreover, the width of the low transmittance range increases as the damping coefficient η increases. For experimental studies of wave transmission in soft metamaterials exhibiting damping, interested readers are referred to the works of [16,44], considering relatively low frequencies. Finally, we note that the analysis of dispersion and wave manipulation is built on the assumption that all unit cells in the metamaterial experience the same intensity of the magnetic field. This may not be the case for the finite-size metamaterial, where the magnetic field may be inhomogeneous, leading to different responses of the unit cells. This is not necessarily unfordable, as, for example, these differences can be potentially utilized to achieve vibration attenuation in a broad frequency regime. In this scenario, the resonators in the unit cells undergo varying degrees of rotational deformation, thus, generating resonance effects at different operating frequencies. Consequently, a broad frequency regime superimposed by the multiple local resonant BGs may be generated.

3. Conclusions

We have proposed an hMAE-based metamaterial with magnetically tunable local resonant BG. The design strategy utilizes the transformative ability of hMAEs coupled with the local resonant metamaterial characteristics. The interaction between the hMAE intrinsic magnetization and activation gives rise to the unusual asymmetric mechanical behavior (with the total Cauchy stress being asymmetric). The complex magneto-mechanical coupling and, hence, the metamaterial performance can be tailored through tuning the microstructure. For instance, the microstructure can be designed to exhibit snap-through and bistable behavior triggered by magnetic field-induced body torque. The localized deformed microstructure can be locked in and retained, even after removing the activating magnetic field. Thanks to the dramatic microstructure switches, the metamaterial exhibits rich tunability in its mechanical stiffness and local resonant BG. We note that the hMAE properties offer the intriguing potential of the asymmetric elastic metamaterials – stemming from the interaction of the external magnetic field and initially magnetized hMAE phases – extending the potential application beyond the local resonant BG phenomenon. For example, the asymmetric metamaterials can be exploited to induce polarity and chirality – two extra degrees of freedom of the elasticity tensor – potentially enabling elastic cloaking [45,46].

Declaration of competing interest

The authors declare that they have no known competing financial interests or personal relationships that could have appeared to influence the work reported in this paper.

Data availability

Data will be made available on request.

Acknowledgments

QZ thanks the support of the National Natural Science Foundation of China through Grant No. 12002030. SR thanks for the support of the European Research Council (ERC) through Grant No. 852281- MAGIC.

References

[1] Z. Liu, X. Zhang, Y. Mao, Y.Y. Zhu, Z. Yang, C.T. Chan, P. Sheng, Locally resonant sonic materials, Science 289 (2000) 1734.
[2] D. Elser, U.L. Andersen, A. Korn, O. Gloeckl, S. Lorenz, C. Marquardt, G. Leuchs, Reduction of guided acoustic wave Brillouin scattering in photonic crystal fibers, Phys. Rev. Lett. 97 (2006) 133901.
[3] H. Liu, Q. Zhang, K. Zhang, G. Hu, H. Duan, Designing 3D digital metamaterial for elastic waves: From elastic wave polarizer to vibration control, Adv. Sci. 6 (2019) 1900401.
[4] Q. Zhang, D. Guo, G. Hu, Tailored mechanical metamaterials with programmable quasi-zero-stiffness features for full-band vibration isolation, Adv. Funct. Mater. 31 (2021) 2101428.
[5] Q. Zhang, K. Zhang, G. Hu, Tunable fluid-solid metamaterials for manipulation of elastic wave propagation in broad frequency range, Appl. Phys. Lett. 112 (2018) 221906.
[6] O.R. Bilal, A. Foehr, C. Daraio, Bistable metamaterial for switching and cascading elastic vibrations, Proc. Natl. Acad. Sci. USA 114 (2017) 4603.
[7] R. Zhu, X.N. Liu, G.K. Hu, C.T. Sun, G.L. Huang, Negative refraction of elastic waves at the deep-subwavelength scale in a single-phase metamaterial, Nature Commun. 5 (2014) 5510.
[8] Z. Wang, Q. Zhang, K. Zhang, G. Hu, Tunable digital metamaterial for broadband vibration isolation at low frequency, Adv. Mater. 28 (2016) 9857.
[9] O.R. Bilal, A. Foehr, C. Daraio, Reprogrammable phononic metasurfaces, Adv. Mater. 29 (2017) 1700628.
[10] G. Memoli, M. Caleap, M. Asakawa, D.R. Sahoo, B.W. Drinkwater, S. Subramanian, Metamaterial bricks and quantization of meta-surfaces, Nature Commun. 8 (2017) 14608.
[11] P. Wang, L. Lu, K. Bertoldi, Topological phononic crystals with one-way elastic edge waves, Phys. Rev. Lett. 115 (2015) 104302.

[12] A. Foehr, O.R. Bilal, S.D. Huber, C. Daraio, Spiral-based phononic plates: From wave beaming to topological insulators, Phys. Rev. Lett. 120 (2018) 205501.
[13] Y. Chen, X. Liu, G. Hu, Topological phase transition in mechanical honeycomb lattice, J. Mech. Phys. Solids 122 (2019) 54.
[14] Q. Zhang, Y. Chen, K. Zhang, G. Hu, Dirac degeneracy and elastic topological valley modes induced by local resonant states, Phys. Rev. B 101 (2020) 014101.
[15] L. Braverman, C. Scheibner, B. VanSaders, V. Vitelli, Topological defects in solids with odd elasticity, Phys. Rev. Lett. 127 (2021) 268001.
[16] P. Wang, F. Casadei, S. Shan, J.C. Weaver, K. Bertoldi, Harnessing buckling to design tunable locally resonant acoustic metamaterials, Phys. Rev. Lett. 113 (2014) 014301.
[17] Y.-F. Wang, Y.-Z. Wang, B. Wu, W. Chen, Y.-S. Wang, Tunable and active phononic crystals and metamaterials, Appl. Mech. Rev. 72 (2020) 040801.
[18] S. Palagi, A.G. Mark, S.Y. Reigh, K. Melde, T. Qiu, H. Zeng, C. Parmeggiani, D. Martella, A. Sanchez-Castillo, N. Kapernaum, Structured light enables biomimetic swimming and versatile locomotion of photoresponsive soft microrobots, Nature Mater. 15 (2016) 647.
[19] R.M. Erb, R. Libanori, N. Rothfuchs, A.R. Studart, Composites reinforced in three dimensions by using low magnetic fields, Science 335 (2012) 199.
[20] E. Acome, S.K. Mitchell, T. Morrissey, M. Emmett, C. Benjamin, M. King, M. Radakovitz, C. Keplinger, Hydraulically amplified self-healing electrostatic actuators with muscle-like performance, Science 359 (2018) 61.
[21] T.F. Tian, W.H. Li, Y.M. Deng, Sensing capabilities of graphite based MR elastomers, Smart Mater. Struct. 20 (2011) 025022.
[22] Y. Li, J. Li, W. Li, H. Du, A state-of-the-art review on magnetorheological elastomer devices, Smart Mater. Struct. 23 (2014) 123001.
[23] S.-Y. Tang, X. Zhang, S. Sun, D. Yuan, Q. Zhao, S. Yan, L. Deng, G. Yun, J. Zhang, S. Zhang, W. Li, Versatile microfluidic platforms enabled by novel magnetorheological elastomer microactuators, Adv. Funct. Mater. 28 (2018) 1705484.
[24] M.A. Moreno-Mateos, M. Hossain, P. Steinmann, D. Garcia-Gonzalez, Hybrid magnetorheological elastomers enable versatile soft actuators, Npj Comput. Mater. 8 (2022) 162.
[25] S. Rudykh, K. Bertoldi, Stability of anisotropic magnetorheological elastomers in finite deformations: A micromechanical approach, J. Mech. Phys. Solids 61 (2013) 949.
[26] A. Goshkoderia, S. Rudykh, Stability of magnetoactive composites with periodic microstructures undergoing finite strains in the presence of a magnetic field, Composites B 128 (2017) 19.
[27] A. Goshkoderia, V. Chen, J. Li, A. Juhl, P. Buskohl, S. Rudykh, Instability-induced pattern formations in soft magnetoactive composites, Phys. Rev. Lett. 124 (2020) 158002.
[28] P. Pathak, N. Arora, S. Rudykh, Magnetoelastic instabilities in soft laminates with ferromagnetic hyperelastic phases, Int. J. Mech. Sci. 213 (2022) 106862.
[29] G. Bertotti, Hysteresis in Magnetism: For Physicists, Materials Scientists, and Engineers, Gulf Professional Publishing, 1998.
[30] G.Z. Lum, Z. Ye, X. Dong, H. Marvi, O. Erin, W. Hu, M. Sitti, Shape-programmable magnetic soft matter, Proc. Natl. Acad. Sci. USA 113 (2016) E6007.
[31] Y. Kim, H. Yuk, R. Zhao, S.A. Chester, X. Zhao, Printing ferromagnetic domains for untethered fast-transforming soft materials, Nature 558 (2018) 274.
[32] R. Zhao, Y. Kim, S.A. Chester, P. Sharma, X. Zhao, Mechanics of hard-magnetic soft materials, J. Mech. Phys. Solids 124 (2019) 244.
[33] D. Yan, A. Abbasi, P.M. Reis, A comprehensive framework for hard-magnetic beams: Reduced-order theory, 3D simulations, and experiments, Int. J. Solids Struct. 257 (2021) 111319.
[34] S.M. Montgomery, S. Wu, X. Kuang, C.D. Armstrong, C. Zemelka, Q. Ze, R. Zhang, R. Zhao, H.J. Qi, Magneto-mechanical metamaterials with widely tunable mechanical properties and acoustic bandgaps, Adv. Funct. Mater. 31 (2020) 2005319.
[35] D. Yan, M. Pezzulla, L. Cruveiller, A. Abbasi, P.M. Reis, Magneto-active elastic shells with tunable buckling strength, Nature Commun. 12 (2021) 2831.
[36] T. Chen, M. Pauly, P.M. Reis, A reprogrammable mechanical metamaterial with stable memory, Nature 589 (2021) 386.
[37] J. Tang, B. Sun, Reprogrammable shape transformation of magnetic soft robots enabled by magnetothermal effect, Appl. Phys. Lett. 120 (2022) 244101.
[38] D. Garcia-Gonzalez, M. Hossain, Microstructural modelling of hard-magnetic soft materials: Dipole–dipole interactions versus Zeeman effect, Extreme Mech. Lett. 48 (2021) 101382.
[39] W. Hu, G.Z. Lum, M. Mastrangeli, M. Sitti, Small-scale soft-bodied robot with multimodal locomotion, Nature 554 (2018) 81.
[40] L. Wang, D. Zheng, P. Harker, A.B. Patel, C.F. Guo, X. Zhao, Evolutionary design of magnetic soft continuum robots, Proc. Natl. Acad. Sci. USA 118 (2021) e2021922118.
[41] Q. Zhang, S. Rudykh, Magneto-deformation and transverse elastic waves in hard-magnetic soft laminates, Mech. Mater. 169 (2022) 104325.
[42] B. Li, W. Yan, Y. Gao, Tunability of band gaps of programmable hard-magnetic soft material phononic crystals, Acta Mech. Solida Sin. 35 (2022) 719.
[43] M. Mooney, The viscosity of a concentrated suspension of spherical particles, J. Colloid Sci. 6 (1951) 162.
[44] N. Gao, J. Li, R.H. Bao, W.Q. Chen, Harnessing uniaxial tension to tune Poisson's ratio and wave propagation in soft porous phononic crystals: an experimental study, Soft Matter 15 (2019) 2921.
[45] H. Nassar, Y.Y. Chen, G.L. Huang, Polar metamaterials: A new outlook on resonance for cloaking applications, Phys. Rev. Lett. 124 (2020) 084301.
[46] H.K. Zhang, Y. Chen, X.N. Liu, G.K. Hu, An asymmetric elastic metamaterial model for elastic wave cloaking, J. Mech. Phys. Solids 135 (2020) 103796.